Smart Rocks and Wireless Communication Systems for Real-Time Monitoring and Mitigation of Bridge Scour
(Progress Report No. 6)

Contract No: RITARS-11-H-MST
(Missouri University of Science and Technology)

Ending Period: December 31, 2012

PI: Genda Chen
Co-PIs: David Pommerenke and Rosa Y. Zheng

Program Manager: Mr. Caesar Singh

Submission Date: January 15, 2013

TABLE OF CONTENTS

EXECUTIVE SUMMARY

In the sixth quarter, the laboratory and field test data documented in the previous quarterly reports continued to be analyzed for useful information in engineering design and maintenance. In addition, the passive and active smart rocks remained at the U.S. Highway 63 – Gasconade River Bridge site were revisited about 10 weeks after the initial deployment to investigate the long-term performance of smart rocks in water. To better interpret the test data obtained in the FHWA Hydraulic Engineering Lab, a large database of characteristic data with a single magnet was developed when the measurement distance and the magnet polarity changed. The previous digital signal processing (DSP) algorithm was further investigated and expanded to either improve its performance or accommodate new applications. In particular, an attempt was made to use the same algorithm both for magneto-inductive and acoustic communication techniques.

For static magnetic field measurements, a scenario study was conducted to compose the scour depth time history (scour evolution) of a passive smart rock by combining the intensity-time relation obtained during the pier model tests at the FHWA Hydraulics Engineering Laboratory with the characterisitic intensity-distance curves at certain polarities of a magnet as developed from the calibration tests. In the following quarter, the calibration tests will be repeated to refine the characteristic intensity-distance curves. More importantly, a localization algorithm will be developed to locate the rock based on the three measurements at three base stations.

For active smart rocks with magneto-inductive communication, various smart rock modules were packaged into two boxes and the active smart rocks deployed in September 2012 were revisited to understand their long-term performance. The field test data indicated that both deployed rocks were functional with strong communication signals. In addition, a new real-time digital signal processing method and algorithm was developed based on a moving-window wake-up pulse identification technique in time domain. The method and algorithm was tested with the simulated data packet from a smart rock in the laboratory. In the following quarter, the new method will be further developed to accommodate low frequency input and then applied in field measurements.

For active smart rocks with acoustic communication, various modules were also packaged into transmission and receiving boxes. In addition, a real-time digital signal processing method with wake-up signal identification by a pulse correlation technique in frequency domain was tested and verified to a satisfactory accuracy.

I - TECHNICAL STATUS

I.1 ACCOMPLISHMENTS BY MILESTONE

The measured data from laboratory and field tests continued to be processed and analyzed in this quarter. The field experience with two bridge tests allowed the team to identify technical improvements of the initial versions of active and passive sensors. Some modifications of active sensors already began. A teleconference with Advisory Committee was held on December 3, 2012.

Task 1.1 Optimal Passive Smart Rock – Engineering Design and Validation of DC Magnetic Passive Smart Rocks

Test Procedure and Results: The magnetic intensity was measured as a magnet moved vertically sway from the magnetometer as illustrated in Fig. 1a. At each location, the magnet was rotated about x-, y-, and z-axis, respectively, as visualized in Fig. 1b.

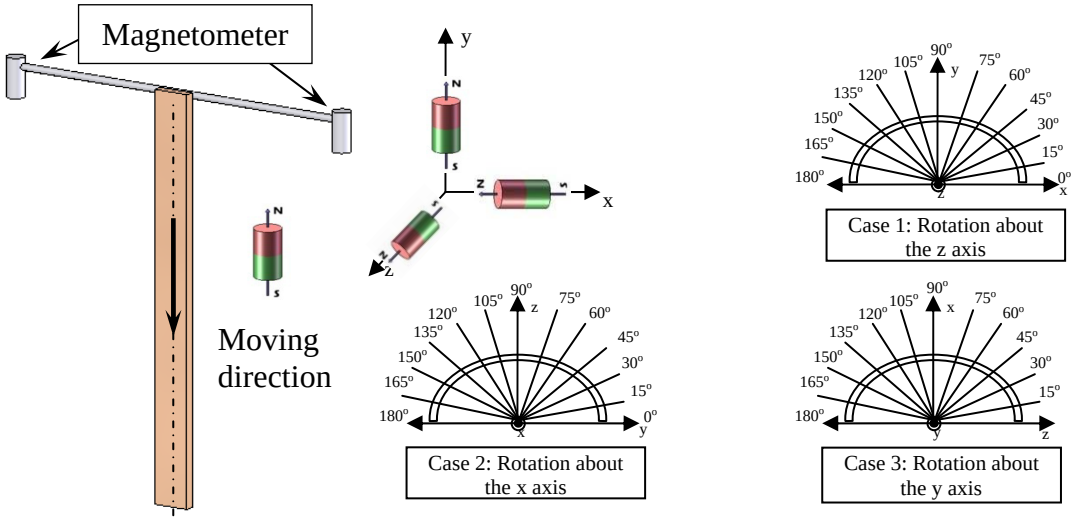

(a) Initial test setup (b) Axes orientation and various test cases

Fig. 1 Strength – distance correlation test setup with 15° rotations of magnet about three primary axes and vertical change in 7.62 cm increments.

The magnet moved vertically in 76.2 mm increments from 0 to 762 mm and 152.4 mm increments from 762 to 1524 mm away from the magnetometer. At each location, the magnet was rotated about the respective axis (x-, y-, or z-) in 15° increments. A total number of 624 unique orientations were evaluated. This test was performed to simulate the movement of a smart rock at a bridge pier during a scour event.

Figs. 2a through 2c display the intensity-to-distance correlation for each angle measurement about each axis in the desired range, approximately 38 – 70 cm (the actual distance away from the magnetometer during laboratory testing at the FHWA Hydraulics Lab). When the magnet is

oriented within the strong area associated with the axis of rotation, the corresponding graph represents the decaying trend associated with the intensity-to-distance correlation. It has been concluded that the local discrepancies in the graphs, i.e. the graphs that do not follow the expected trend, are due to the method of data acquisition. Instead of collecting one orientation angle along the test path at one time, the orientation was changed from 0 to 180 degrees in 15 degree increments before continuing along the test path. Because of this and the fact that the orientation was manually managed it is possible for the assumed angle to be slightly off and therefore creating the unexpected trend shown.

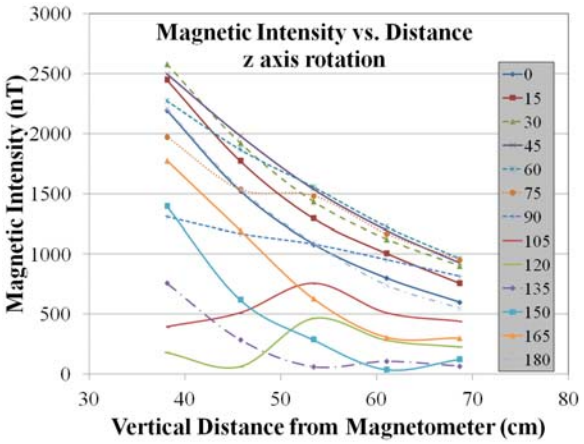

(a) Magnetic rotation along *z* axis

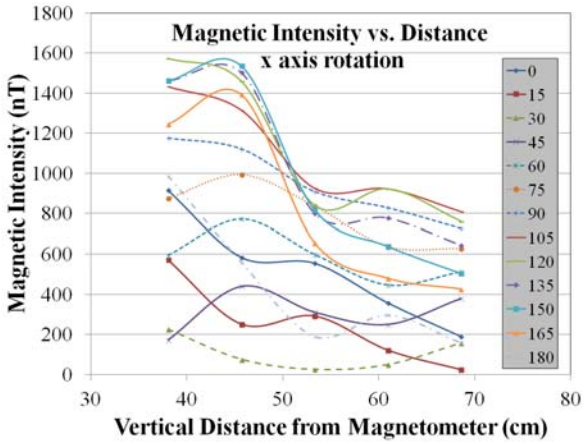

(b) Magnetic rotation along *x* axis

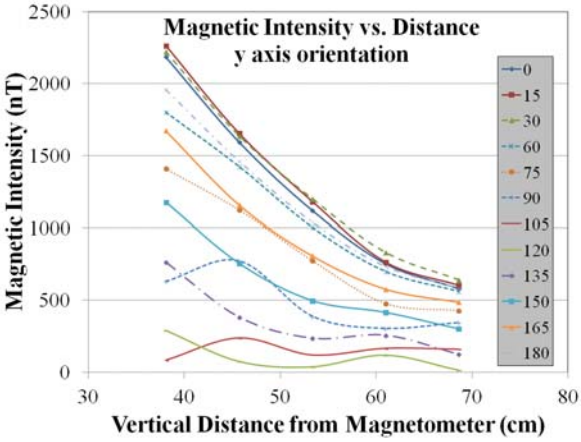

(c) Magnetic rotation along *y* axis

Fig. 2 Intensity change due to increased distance for various magnetic orientations.

As clearly illustrated in Figs. 3a through 3c, the orientation of magnet has a large impact on the strength of magnetic field when the magnet at certain positions is rotated about x-, y- and z-axis, respectively. As expected, an increased depth results in a decreased magnetic intensity regardless of which axial rotation was being tested. Each orientation also shares the same general sinusoidal trend as well. Rotating about the z- or y-axis only a slight amplitude adjustment would need to be made. However, rotation about the x-axis shows not only a significant amplitude difference but also a phase shift of nearly 60 degree. With such database of characteristic behaviors of the tested magnet, the aim is to be able to simulate the graph acquired from the scour testing event.

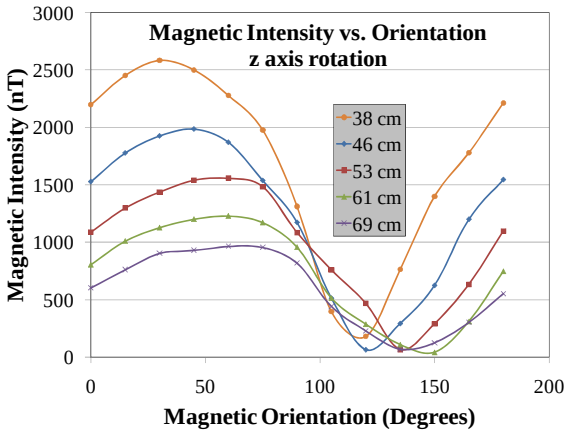

(a) Magnetic rotation about the z axis

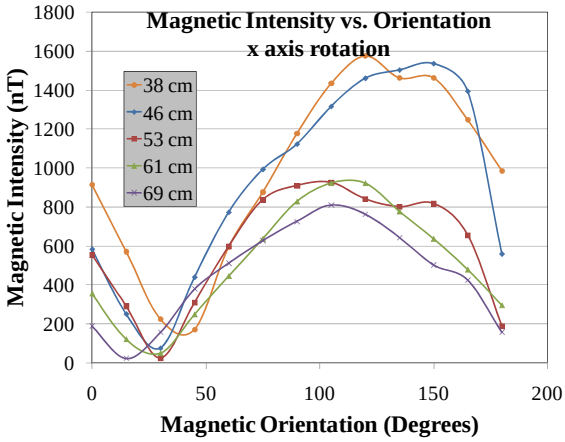

(b) Magnetic rotation about the x axis

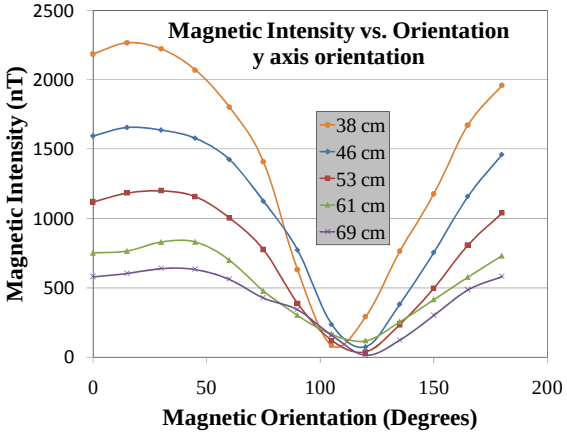

(c) Magnetic rotation about the y axis

Fig. 3 Effects of magnetic orientation at fixed vertical distances from 38 to 69 cm.

Analytical Results Compared to Laboratory Results: During previous quarters of the project the research group visited FHWA Hydraulics Lab to test the passive smart rock in a scour simulation flume. Throughout this test magnetic intensity readings were collected with the magnetometer at various time increments. This data was processed and displayed in the graph in Fig. 4a. The magnetometer was located at the top of the small scale pier directly over the smart rock and data was collected approximately every 10-15 minutes during the scour event.

Fig. 4a also shows a graph derived from the characteristic behavior database. Table 1 displays the curve fitted data collected from the characteristic behavior database. The axis of orientation, column one, indicates which chart (Figs. 2a through 2c) to look at for the given point; the second column, angle of orientation, indicates the graph used from the afore mentioned chart; and the fifth column, interpolation points, indicates which two measured points were used for interpolation to obtain the corresponding distance from the magnetometer. All interpolations were assumed to be straight lines between two points.

Fig. 4b is the resulting scour depth over time relationship. It is not possible to obtain intermediate scour depths during the scour test to compare with the characteristic behavior. However, the trend shown seems to be representative of typical scour events. As the scour depth increases the

rate of scour decreases as shown. While this derived solution is not unique (other orientations could be found for the tested case) it does exemplify the potential to predict and discern the difference between an orientation effect and a distance effect.

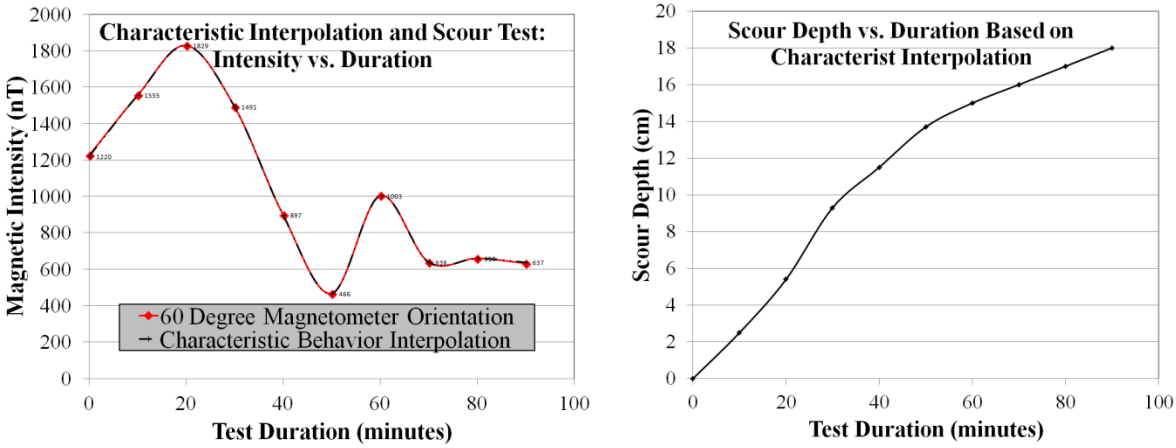

(a) Characteristic behavior versus scour test (b) Simulation from characteristic behavior

Fig. 4 Analytical simulation of testing results derived from characteristic behavior.

Table 1 – Characteristic behavior curve fit data compared to scour test measurements

Axis of Orientation	Angle of Orientation	Scour Depth	Time of Measurement	Interpolation Points	Characteristic Measurement	Actual Test Results
Units	Degrees	cm	minutes	nT	nT	nT
z	90	0	0	1310, 1171	1220	1225
z	75	2.5	10	1975, 1537	1555	1555.3
z	45	5.4	20	1984, 1540	1829	1828.5
z	75	9.3	30	1537, 1484	1491	1491.3
y	75	11.5	40	1184, 766.5	897	897.4
x	0	13.7	50	554, 356	466	466.2
z	180	15	60	1084, 955.4	1003	1003.2
y	165	16	70	808, 578	638	637.9
x	150	17	80	837, 637	659	659.5
x	150	18	90	637	637	632.3

Task 1.2 Steel Interferences to Magnetic Measurements – Noise Level, Data Cleansing and Engineering Interpretation with Passive Rocks Submitted

The previous report already indicated that the gradient measurement mainly removed the Earth's magnetic field. There is no clear sign of indication that the noise level in the gradient readings was reduced by the subtraction between the readings from two sensor heads of a magnetometer.

Task 2.1 Active Smart Rocks with Embedded Controllable Magnets or with Embedded Electronics – Engineering Design and Validation of Active Smart Rocks Submitted

No further work was done with embedded controllable magnets during the past quarter.

Task 2.2(a) Magneto-Inductive Communications – Engineering Design and Validation of Magneto-Inductive Transponders Submitted

Active Smart Rock v3 The new generation of Smart Rock electronic board (v.3) was designed November 2012. The new design provides following updates:

- Upgraded PIC16LF1829 microcontroller
- Gyroscope (ST Microelectronics L3G4200D)
- On-board flash memory (Atmel AT24C1024B-TH-B)
- Alternative current-driven solution for antenna excitation
- Improvements and fixes

Fig. 4 shows photo of the assembled Smart Rock v.3 board with noted main IC components. The new microcontroller provides a larger program space and more pins for interrupt/control processing. The Gyroscope is a new addition for further code development of a Smart Rock move trajectory recovery. It is ST Microelectronics IC, similar to the accelerometer used on the board, accessible by I2C bus.

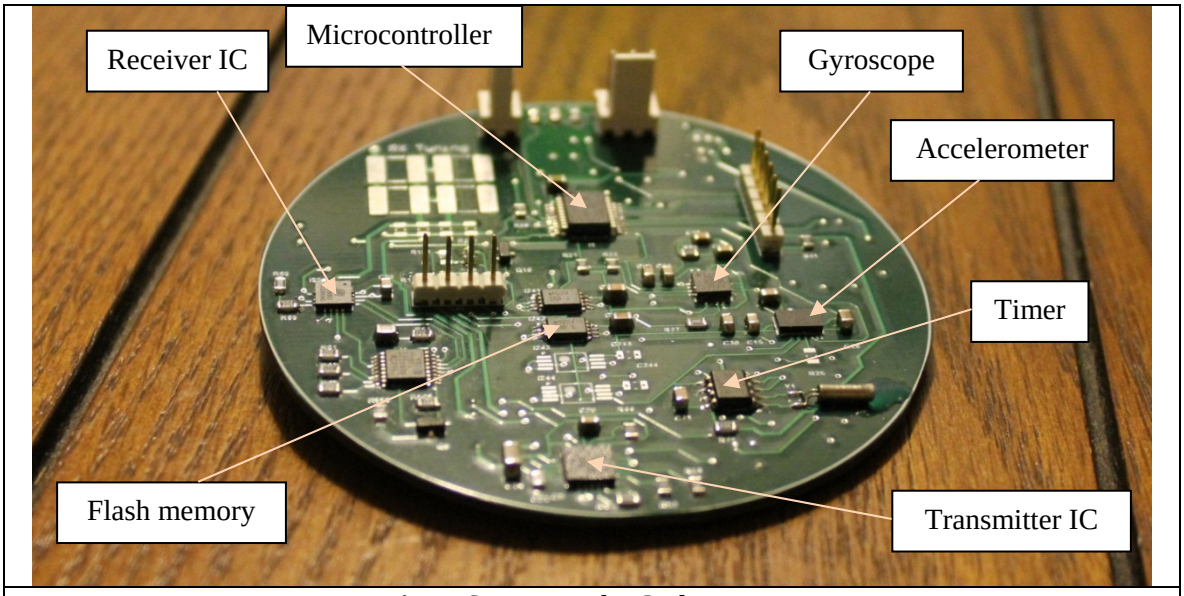

Fig. 5 Smart Rock v3 electronics

Smart Rock v.3 supports up-to four flash memory ICs, accessible by I2C with Atmel AT24C1024B-TH-B, each providing 1 MB memory space. Depending on the Smart Rock operation mode, it is enough for up to few thousands Smart Rock sensors data records to be stored. Two operation scenarios are considered for memory usage:

- High-rate data recording during relatively fast movement
- Data storage for Smart Rock inter-sensors network communication (RSSIs, IDs, Sensors)

The Smart Rock v.3 boards provide two ways for antenna excitation:

- Voltage driven (used in Smart Rock v.2.4, transmission own-design circuitry with H-bridge), preferable for acoustic transducers usage
- Current driven (used in Smart Rock v2.5, 125 KHz antenna driver transmitter IC), preferable for RF magneto-inductive link

The specific scheme can be selected using a jumper switch in application. Providing both configurations on the same board is one step towards the implementation of both RF and acoustic solutions if they are proven effective towards the end of this project.

The Smart Rock v.3 board maintains a small size (76 mm in diameter), making it possible to use the boards both in laboratory and field environments. When possible, IC components are selected to be in SOP packages and passive components (resistors/capacitors) are at least 0806 size, which makes it easier to assemble as compared to Smart Rock 2.4/2.5 designs. However a few IC components (Gyro, Accelerometer, and Receiver) are only available in QFN package. The components cost per board is below $100. Initially three boards were assembled, after testing few minor design issues were detected and fixed in Smart Rock v3.1 design. Nine more boards were manufactured for further testing / development / deployment.

Repeated Bridge Tests Two active Smart Rocks were deployed at US 63 Highway Bridge in September 2012. After a communication link was established with the sensors embedded in the rocks, the smart rocks were left in the river. On November 30, 2012, the field test was repeated. Communication with sensors was successfully performed from the bridge deck at about 19.8 m distance. Both sensors flawless responded to the base station wake up signals. Fig. 6 shows the test setup in the back of a truck with antennas located in the bridge side. Fig. 7 shows the wake up signal sent from the base station followed by response from one of the sensors.

Fig. 6 US 63 Bridge – revisit

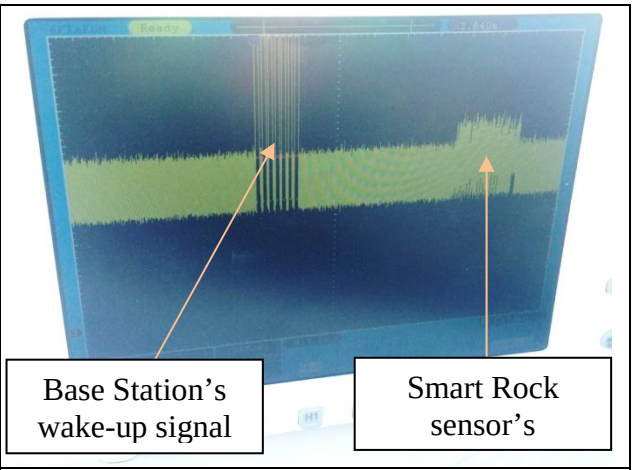

Fig. 7 Scope signal observation

Figs. 8 and 9 show the stored communication signals for Rock A and Rock B. The response signal from Rock B is significantly stronger than Rock A, indicating a difference in distance from the base station. Further tests will be performed for localization algorithms development. The performed tests validated the relatively long-term stability of Smart Rock electronics design and waterproof enclosing design for Smart Rock sensor shell.

Digital Signal Processing Demodulator Previous reports and activities with Active Smart rocks communication were performed using analog base-station / filter / demodulator units. Switch to digital signal processing (DSP) is a promising new development, providing better sensitivity and filtering features that will result in a more stable communication link and possibility to achieve larger distances for Smart Rock data acquisition.

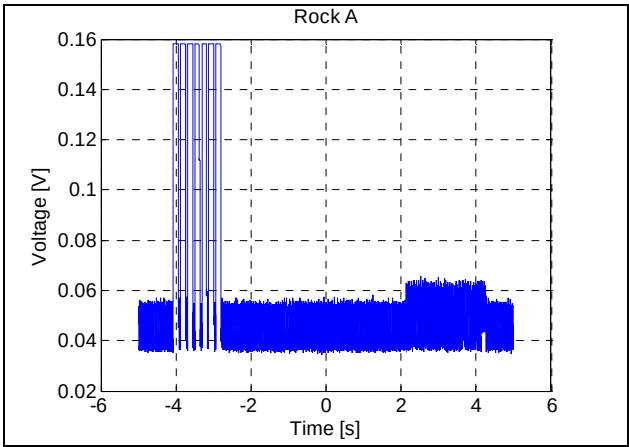

Fig. 8 Communication with Rock A

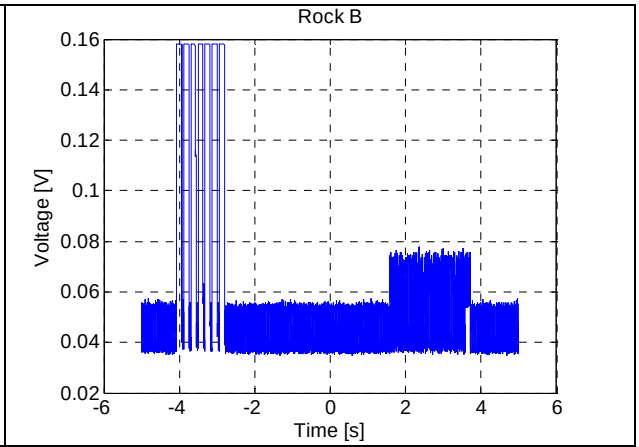

Fig. 9 Communication with Rock B

The DSP demodulator for Smart Rock data was implemented. This section of the report describes the implemented algorithm and test results. The Smart Rock board microcontroller operates on a 125 KHz frequency and is capable of generating an amplitude-shift keying (ASK) modulated signal with a configurable baud rate. The baud rate, however, cannot be arbitrarily specified and must be selected to be Fosc/(4*(N+1)), where N is an int8 value. The carrier frequency of an output modulated signal can be configured as Fosc divided by any of [2, 4, 8, 16, 32, 64, 128] values.

A real-time DSP demodulator algorithm was developed and tested with a packet of simulated data sent by a Smart Rock module, as shown in Fig. 10. The packet of data include a long carrier burst (~0.18 s), a preamble marker 1111111010010001, a set of alternating 0-1 bits and coded data from Accelerometers and Magnetometers. More 0-1 alternating bits are repeated prior to a carrier wrap-up. The header/preamble data between 0.18 and 0.3 s is detailed in Fig. 11.

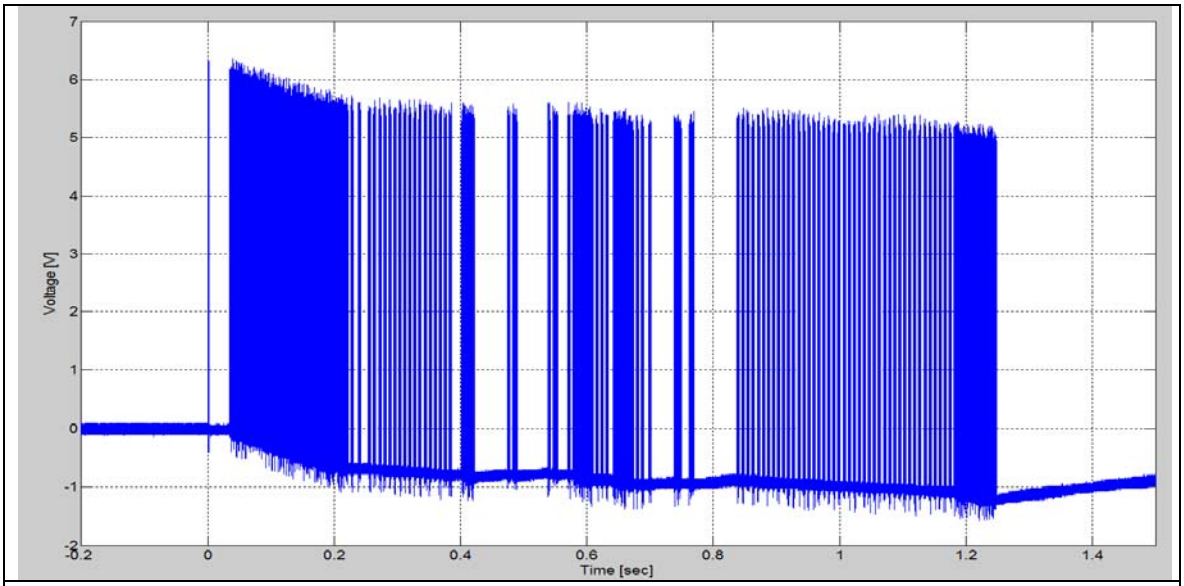

Fig. 10 Signal sent by a Smart Rock module

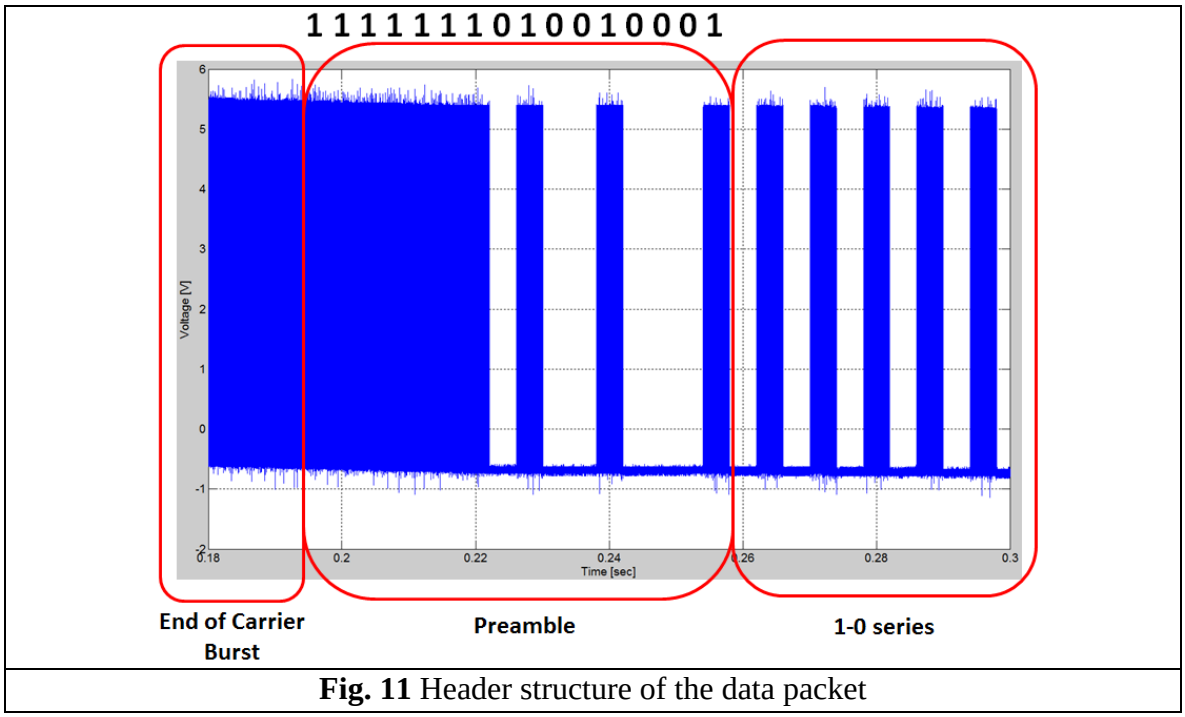

Fig. 11 Header structure of the data packet

The implemented real-time DSP system was then tested with the actual smart rock on-board sensors data. In this case, the output port of the smart rock board (PCB with the original antenna connection interface) was directly connected to the DSP board for data transmission. The accelerometer output data consists of two byte values for each X/Y/Z axis, providing LOW and HIGH bytes of a 16 bit signed integer. After recombination of the Low/High bytes, the accelerometer vector can be obtained as illustrated in Fig. 12a. During the test, the PCB was initially oriented parallel to the ground surface with the 3-aix accelerometer placed on the top side of the board (a dominant positive Z component), then flipped over with the accelerometer placed on the bottom side of the board (a dominant negative Z component), and finally oriented such that the X and Y components are significant.

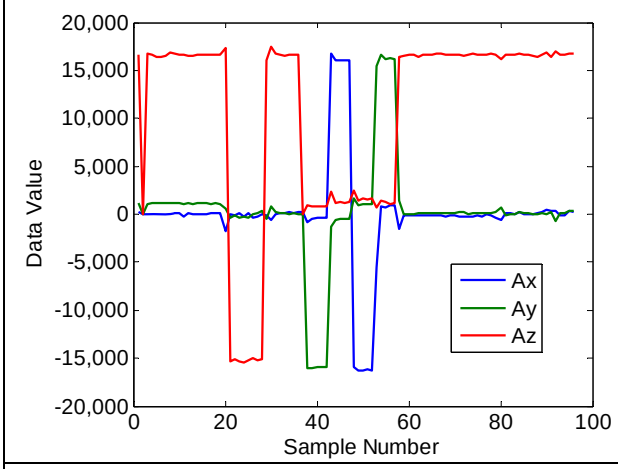

(a) Combined reading of accelerometer output

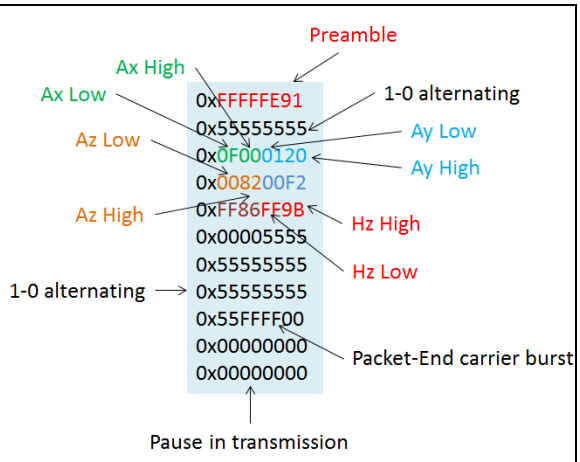

(b) Extraction from the stored output file

Fig. 12 Extraction and recombination of the 3-axis accelerometer output

For actual Smart Rock operations, the data packet contains information from battery meter, accelerometer, magnetometer, gyroscope, and pressure sensor. However, for the real-time DSP code development, only accelerometer data was processed and most of other data-parts were replaced by alternated 1-0 sequences as indicated in Fig. 12b.

Communication Link Modeling For further optimization of the communication link/channel to achieve a larger communication distance, the Grundig AN-200 antennas deployed at the bridge sites as shown in Fig. 13a was modeled as illustrated in Fig. 13b.

(a) Grundig AN-200 antenna

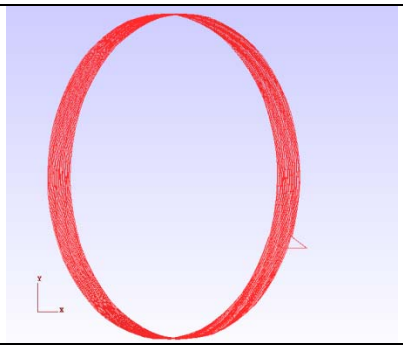

(b) Simulation model

Fig. 13 Modeling of a Grundig AN-200 antenna

The double antenna contains 28 turns of 0.8-mm-diameter wires with 22.7 cm in diameter, resulting an overall height of 2.3 cm. To identify the antenna model parameters, the inductance of the coil was either measured using an LCR-meter or obtained from the analytical solution and the Static 3D modeling in EMC Studio as illustrated in Fig. 13b. The measured, analytical, and numerical inductances are 348, 317, and 349 μH, respectively. With the measured inductance, the capacitance of the transmission and receiving antenna in smart rocks corresponding to an LC-resonance/carrier frequency of 125 kHz is estimated to be 4.64 nF.

In a smart rock, the coil is embedded into a concrete encasement with approximately 0.5 m in diameter so that the antenna is located 15-40 cm above the ground, which could cause detuning of the antenna. To understand how the presence of ground and the rotation of rock shell affect the self-inductance of the coil, a series of simulations were performed numerically. However, the simulation model does not directly represent rolling. Therefore, the center of the antenna is kept on the same height while in rotation. Figs. 14 and 15 demonstrate the change in simulated self-inductance of the coil as a function of rotation angle when the antenna is placed at 30 cm above the ground. It can be observed from Fig. 15 that the ground surface affected the simulated inductance of the coil by approximately 1-2 mH only, corresponding to a frequency detuning by 0.2-0.3 KHz over the free space estimation when a fixed capacitance is used.

The mutual coupling between two identical antennas was then analyzed. For simplification, the transmission antenna was replaced by a 1A impressed current source. Both excitation and receiving antennas are placed such that their centers are on a vertical line, as illustrated in Fig. 16, while the Rx antenna is rotated for polarization loss factor estimation. This configuration is similar to the actual deployment of a smart rock at the bridge site with the communication channel established from the bridge deck. Fig. 17 shows the receiver antenna port model.

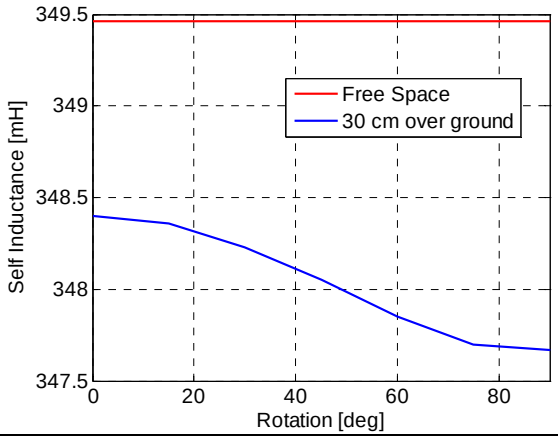

Fig. 14 Coil inductance vs. rotation angle

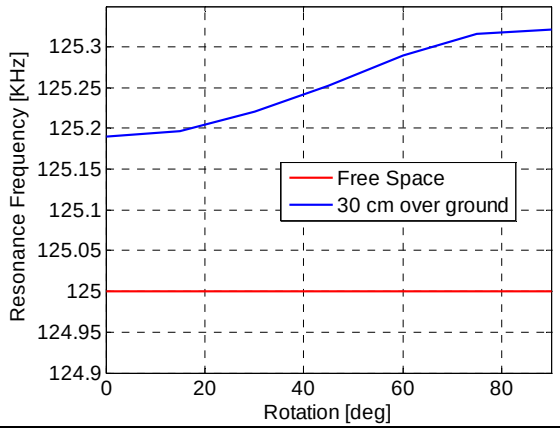

Fig. 15 Resonance drift due to rotation

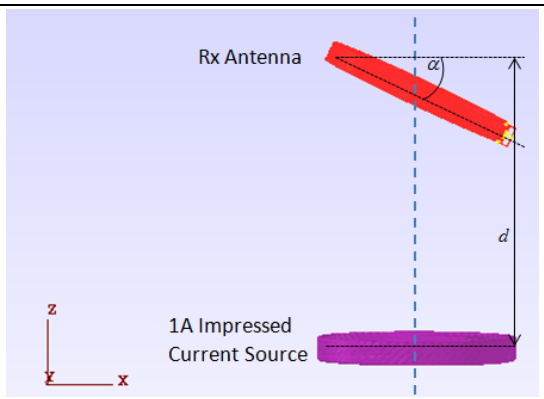

Fig. 16 Antenna orientation sweep

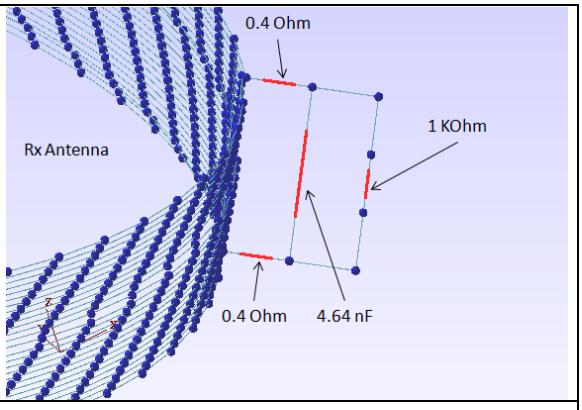

Fig. 17 Receiver antenna port

Pair of 0.4 Ohms in series with the coil represents DC resistance of the coil (the coil wire is generally set as a perfect electrical conductor or PEC). The tuning capacitor (4.64 nF) and load (1 KOhm) were used in simulations, corresponding to the input of pre-amplifier/filter stage of Smart Rock base station hardware unit. The coupled voltage observed at the 1 KOhm resistor is presented in Fig. 18 - Fig. 21, demonstrating effects of the distance between transmission and receiving antennas and the angle of receiving antenna.

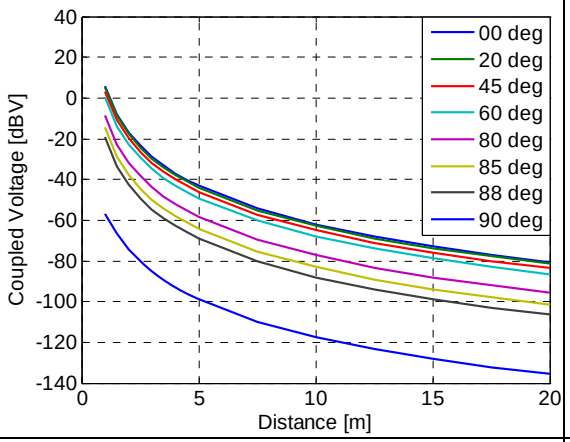

Fig. 18 Coupled voltage vs. distance

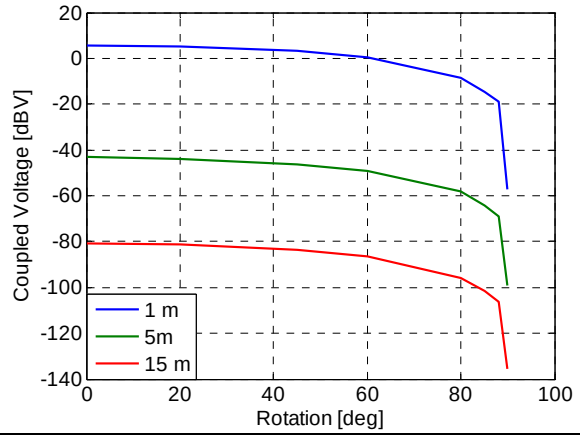

Fig. 19 Coupled voltage vs. rotation angle

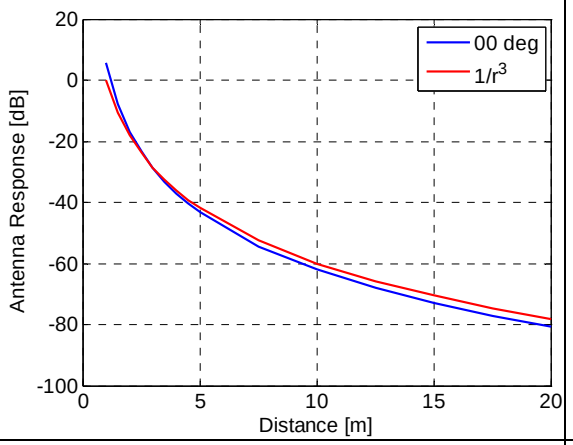

Fig. 20 1/r^3 fit to antenna response

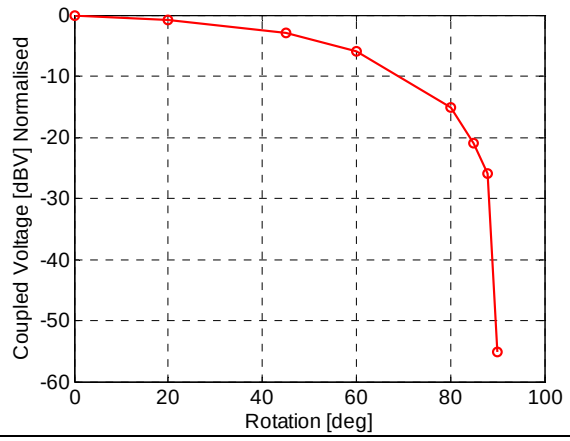

Fig. 21 Normalized voltage vs. rotation angle

It can be clearly seen from Fig. 20 that the antenna response decays with distance by 1/r^3 and has approximately 20 dB change with a 0-85° angular misalignment. If the angular misalignment is below 60°, the signal loss is less than 6 dB.

Task 2.2(b) Acoustic Communications – Engineering Evaluation of Acoustic Communication Systems for Bridge Scour Monitoring

In this quarter, the acoustic communication system has been integrated, thoroughly tested, and duplicated into two sets. The transmitter consists of the 'C6713 board, a digital to analog converter (DAC), a power amplifier and acoustic projector, as shown in Fig. 22a. The receiver consists of two channels of hydrophones, LNA (low-noise amplifier), and ADC (analog to digital converter), interfacing with one 'C6713 board. The hardware has been integrated into two instrument boxes, and two sets of transmitters and receivers have been produced and tested. The testing bench of the transmitter and receiver is shown in Fig. 22b.

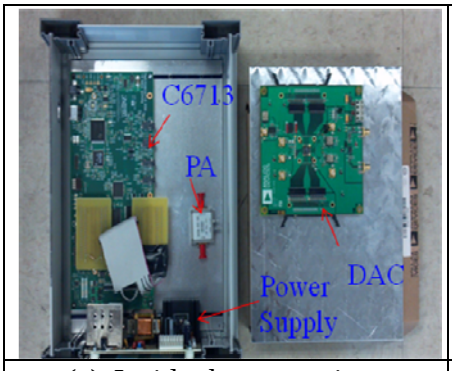

(a) Inside the transmitter

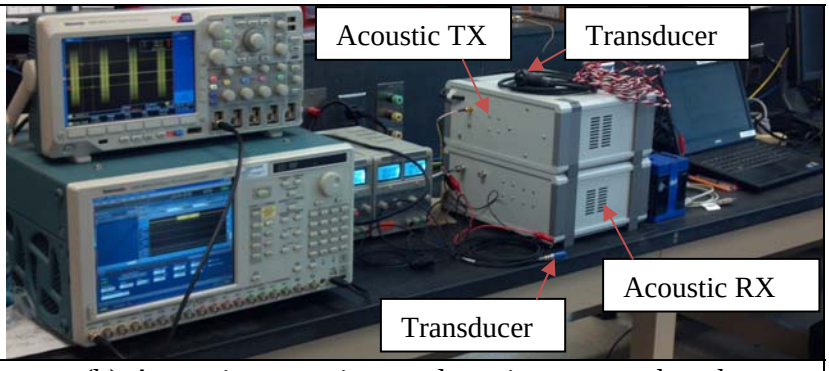

(b) Acoustic transmitter and receiver on test bench

Fig. 22 The integrated acoustic communication system

The transmit signaling and receive detection algorithm are thoroughly tested and finalized. The technical details for hardware configuration are shown in Fig. 23. The Phase Locked Loop (PLL) generates the system clocks for the Central Processing Unit (CPU) and the External Memory

Interface (EMIF). The CPU connects to the Enhanced Direct Memory Access (EDMA) buffers with the address and data buses. Since On-Off Keying (OOK) modulation is used in the communication system, bit 1 is represented by a cosine wave of frequency fc=125 kHz, and bit 0 is represented by DC voltage. The bit rate is set to R= 5 kbps, yielding a signal bandwidth BW=5 kHz. The bit rate can be easily changed to 250 bps, 500 bps or 1.25 kbps. Two EDMA buffers are used to save the waveform values for a bit 1 and a bit 0. A 63-bit maximum-length pseudo-noise (PN) code is used as the ID code and is inserted before the payload bits. The CPU reads the combined data bits from external files/sensors, and toggles the EDMA buffers for transferring the modulated signal to the EMIF. The EMIF works in asynchronous transfer mode and its lowest 12 bits are sent to the DAC. Under the control of Asynchronous Write Enable (AAWE), the bits are converted into the OOK modulated signal. The output of the DAC is in differential current mode and is transformed by a T1-1T transformer into a unipolar voltage mode.

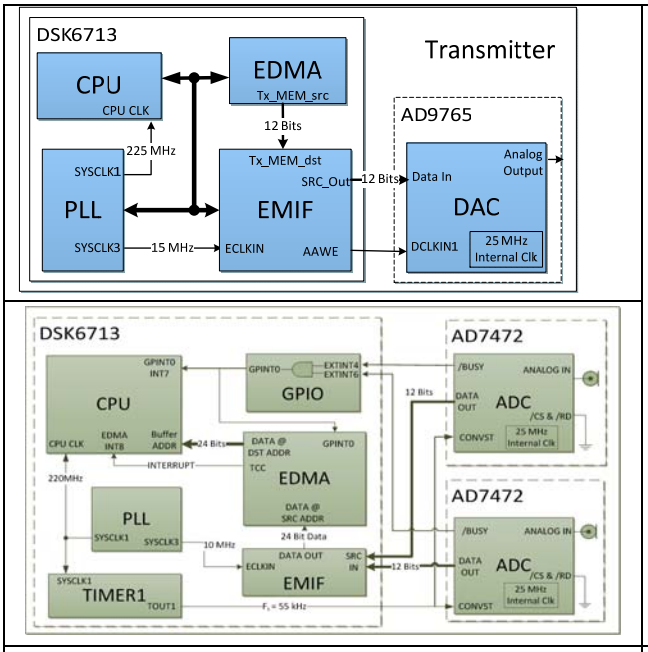

Fig. 23 Signal configuration in DSP hardware implementation of the transmitter and receiver.

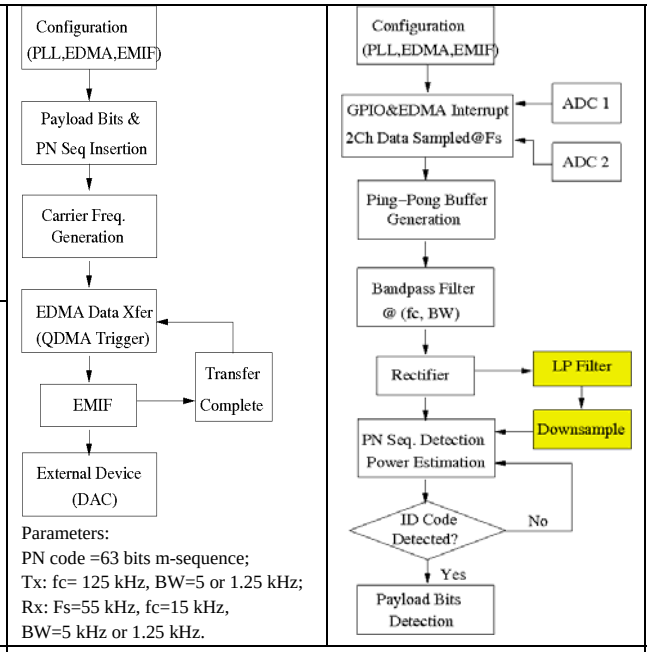

Fig.24 DSP programming flow for the transmitter (left) and receiver (right).

The receiver also uses the PLL for system clock generation. In addition, it uses a Timer to generate an additional clock for the two ADCs. Although the modulated signal has a carrier frequency of fc=125 kHz, we use 55 kHz sampling frequency for the ADCs which yields band-pass sampling with the folded signal centered at 15 kHz. The /BUSY signals from the ADCs indicate that the A/D conversion is finished if /BUSY=0. To receive data from one or two ADCs, the AND logic gate in the GPIO (General Purpose Input/Output) port is used to interrupt the CPU and enable the EDMA. The 12-bit data buses from both ADCs are connected to the EMIF and the 24-bit data samples are transferred to EDMA simultaneously. The EDMA is configured into a Ping-Pong buffer. When the Ping buffer is filled with data samples, the EDMA triggers a hardware interrupt via the TCC (Transfer Complete) port and the service routine switches the data transfer to the Pong buffer. The Ping-Pong buffer toggles back and forth to enable the data processing in frames.

The DSP programming flow is shown in Fig. 24. The transmitter program compiles the cosine wave values at 3MHz rate for bit 1. This is 24 samples per cycle at fc=125 kHz and 24R samples per bit-buffer. The EDMA data transfer uses the QDMA mode to toggle between bit 1 buffer and bit 0 buffer, depending on the input bit value. The TCC (transfer complete) signal controls when to switch the bit value. The receiver program first includes the GPIO and EDMA interrupt service routines to read in the ADC data samples from both channels. Data samples fill in the Ping or Pong buffers alternatively. When the Ping buffer is saving data, the Pong buffer is processed by the receive detection routine, which includes band-pass filtering, full rectifier, low-pass filtering and down sampling if R=250 bps – 1.25 kbps, then follows with PN sequence detection via matched filtering (MF), and signal power estimation via window averaging. The band pass filter is a 69-tap FIR with the normalized center frequency at f=15/55 and bandwidth BW=5/55. The rectifier generates the baseband signal and the matched filter for the PN codes low pass the rectified signal. Once the average signal power over a 63-bit window is detected to be above the noise level, a dynamic threshold is selected according to the signal strength, and the peak at the MF output is searched. If the ID code (PN sequence) matches the desired one, a peak can be detected and the time index gives the bit start. The peak index can be used for synchronization. If the transmission time is available, the peak index can also be used to estimate the propagation time between the transmitter and receiver. Multi-channel receiver can use this to find the Time Difference of Arrival (TDoA) for localization purpose. After the ID code is detected, the payload bits are then detected using 11-point rectangular window averaging. If no peak for the ID code is detected, the program loops back to the PN code detection by shifting the data window further.

Task 3.2 Field Validation Planning and Execution – Field Test Plan and Data Analysis Submitted

As presented in the previous sections, both passive and active smart rocks were tested at two bridge sites.

I.2 PROBLEMS ENCOUNTERED

There are no problems encountered in this quarter. However, the project continued to be delayed for about three months as explained in the previous report. On the other hand, the project expenditure is in general agreement with the project progress.

I.3 FUTURE PLANS

Three subtasks will be executed during the next quarter. A brief description of various activities in each subtask is described below:

Task 1.1 Design, fabricate, and test in laboratory and field conditions DC magnetic sensors with embedded magnets aligned with the earth gravity field. Summarize and document the test results and the performance of passive smart sensors.

Further characteristic behavior mapping data is planned for the next quarter. However, instead of finding the characteristic behavior of the small scale smart rock, the actual bridge scale model behavior will be analyzed and mapped to determine bridge scour depth of the long-term field tests in progress. In addition, the smart rocks placed at the two bridge sites are currently being monitored periodically for long term scour data at full scale bridge locations in Missouri.

Task 1.2 Research, summarize, and document the degree of potential steel interferences to magnetic measurements. Investigate ways to compensate the interference effect and develop a rock localization technique.

Further tests will be conducted in laboratory to characterize how adjacent metals affect the magnetic field measurement.

Task 2.1 Design, fabricate, and test in laboratory and field conditions active smart rocks with embedded controllable magnets or with embedded electronics. Summarize and document the test results and the performance of active smart rocks.

An active smart rock with a magnet fixed in an inner solid ball and placed inside an outer thin-walled open ball was designed with a balanced weight concept. Oil was used to fill the small gap between the inner solid ball and the outer open ball in order to minimize the friction and allow free rotation of the inner ball. An initial version of the smart rock was fabricated and tested with an exterior coil. Due to the unavoidable friction between the solid and open balls, the energy required to rotate the inner ball was considered to be excessive. A further attempt will be made to refine the design in the following quarter.

Task 2.2(a) Design, fabricate, and test in laboratory and field conditions magneto-inductive transponders. Summarize and document the test results and the performance of transponders.

The smart rock was originally programmed to use a carrier frequency of 125 kHz. This is faster than the maximum sample rate of the AIC23 codec of 96 kHz. Due to the uses of hardware filters on the DSP-board and the filters on the AIC23 codec, the lower carrier frequencies were tried (64, 32.125, 31 kHz). However, the filtering on the DSP-board limited the implementation to near-audio frequencies. As such, a carrier frequency of 15.625 kHz was used (125/8 kHz). In smart rock applications, conversion hardware will be designed to effectively change the 125 kHz RF link frequency to any audio-range frequency for further DSP processing.

For better localization, an inter-rock network will be developed to acquire the relative ‘near-field’ received signal strength indicator (RSSI) between a set of rocks as illustrated in Fig. 25. This scheme will improve the accuracy of localization and compensate potential environmental errors.

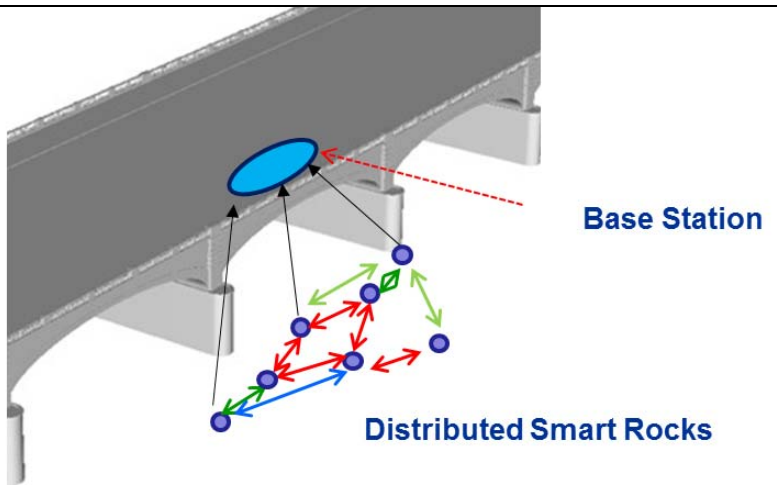

Fig. 25 Inter-rock network concept

In addition, the following topics will be tackled in the following quarter:

- Gyroscope data processing for movement trajectory recovery tests
- Frequency changer development for DSP algorithm application to the actual Smart Rock system
- Implementation of commands protocol to Smart Rock sensors remote reconfiguration
- Magnet flipping circuitry design for the controllable magnet Smart Rocks
- Development of localization schemes

Task 2.2(b) Research, summarize, and document current underwater acoustic transmission practices and required modifications for bridge scour monitoring.

Both transmitter and receiver programs have been thoroughly tested and optimized. In the remaining performance period, the following tasks will be performed, including:

1. Develop the detection method for TDoA using four channel receiver
2. Develop the localization algorithm using TDoA
3. Test the TDoA method and the localization algorithm in field experiment
4. Integrate the DSP transmitter with sensor board and micro-controller
5. Integrate transmitter and receiver together and develop power management circuits.

Task 3.2 Plan and execute the field validation tasks of various prototypes. Analyze the field performance of smart rocks and communication systems.

Initial field tests at two bridge sites were completed. The field test data will be further processed to evaluate the field performance of various technologies.

II – BUSINESS STATUS

II.1 HOURS/EFFORT EXPENDED

The planned hours and the actual hours spent on this project are given and compared in Table 2. In the sixth quarter, the actual hours are more than the planned hours. However, the actual cumulative hours are approximately 66% of the planned hours, corresponding to the project delay starting the third quarter. The cumulative hours spent on various tasks by personnel are presented in Fig. 26.

Table 2 Hours spent on this project

	Planned		Actual	
	Labor Hours	Cumulative	Labor Hours	Cumulative
Quarter 1	752	752	184	184
Quarter 2	752	1504	345	529
Quarter 3	752	2256	381	909
Quarter 4	752	3009	166	1075
Quarter 5	720	3729	721	1877
Quarter 6	720	4449	1069	2946

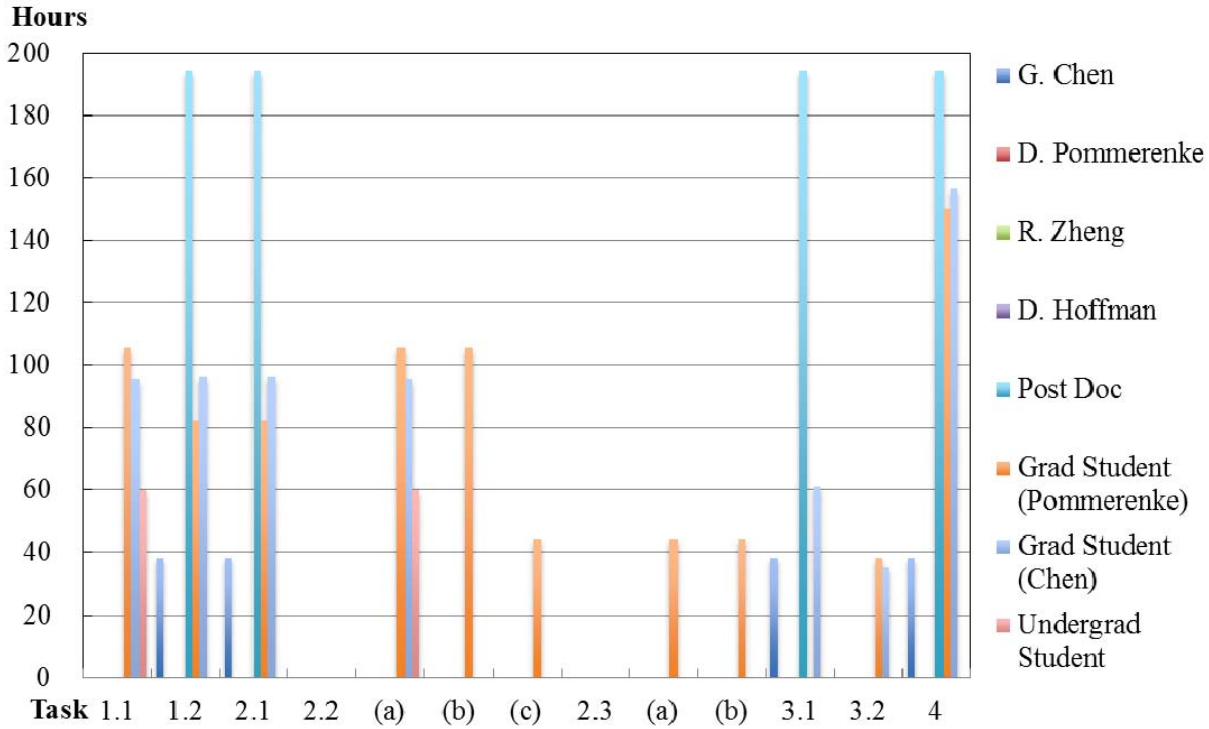

Fig. 26 Cummulative hours spent on various tasks by personnel

II.2 FUNDS EXPENDED AND COST SHARE

The budgeted and expended RITA funds accumulated by quarter are compared in Fig. 27. Approximately 54% of the budget has been spent till the end of sixth quarter. During the sixth quarter, 90% of the budget has been spent. Therefore, the project expenditure in the sixth quarter is in alignment with the budget. The actual cumulative expenditures from RITA and Missouri S&T/MoDOT are compared in Fig. 28. The expenditure from RITA is significantly less than the combined amount from the Missouri S&T and MoDOT.

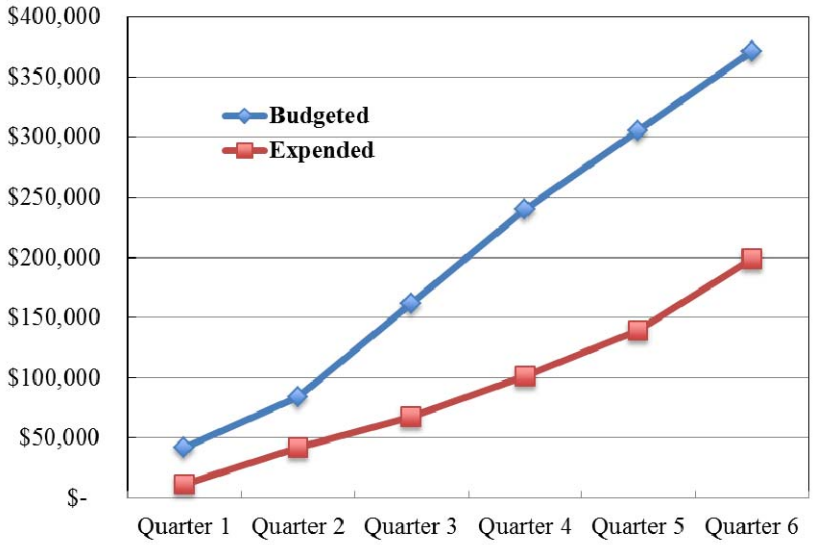

Fig. 27 Comparison of RITA budget and expenditure accumulated by quarter

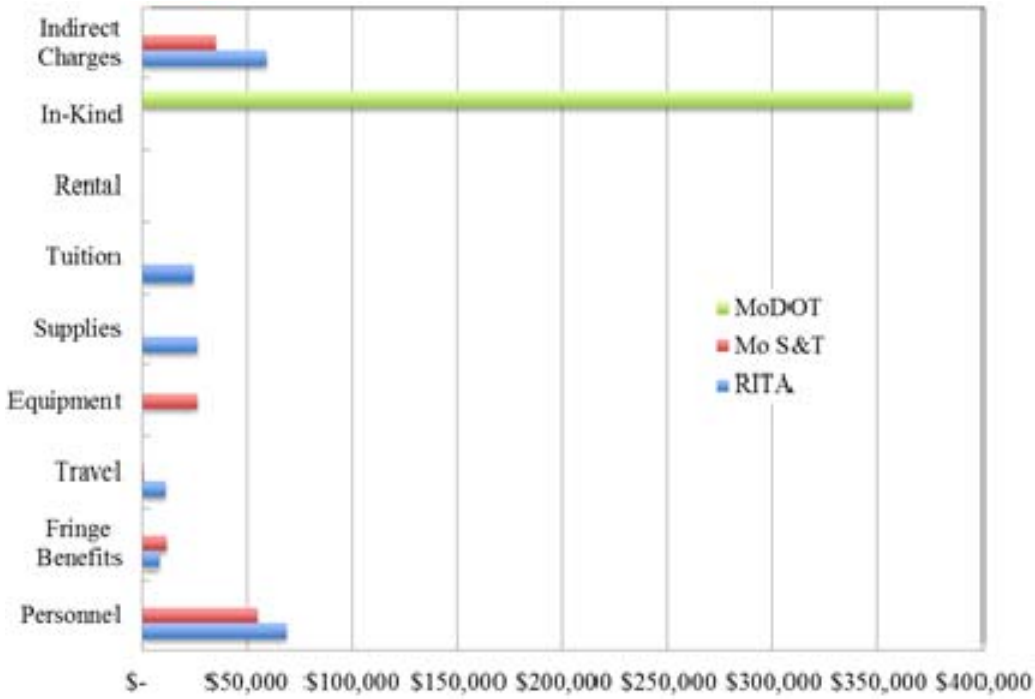

Fig. 28 Cummulative expenditures by sponsor